Solar Phys (2009) 258: 331–341
DOI 10.1007/s11207-009-9406-x

Inferring Small-Scale Flatfields from Solar Rotation

R. Wachter · J. Schou

Received: 19 February 2009 / Accepted: 19 June 2009 / Published online: 21 July 2009

Abstract We present a method to infer small-scale flatfields for imaging solar instruments using only regular-observation intensity images with a fixed field of view. The method is related to the flatfielding method developed by Kuhn, Lin, and Loranz (*Publ. Astron. Soc. Pac*. **103**, 1097 – 1108, 1991), but does not require image offsets. Instead, it takes advantage of the fact that the solar image is changing in the CCD reference frame due to solar rotation. We apply the method to data sets of MDI filtergrams and compare the results to flat fields derived with other methods. Finally, we discuss the planned implementation of this method in the data processing for *Helioseismic and Magnetic Imager* on the *Solar Dynamics Observatory*.

Keywords Helioseismology, observations · Instrumental effects · Cosmic rays, solar · Cosmic rays, galactic

1. Introduction

A flatfield is the instrumental image of a spatially-homogeneous light source. Once known, spatial inhomogeneities in the instrumental response can be corrected for by dividing the obtained images by the flatfield. On small scales, flatfields are generally dominated by the gain variations of the CCD, whereas on larger scales, both CCD features and optical inhomogeneities can be recognized in the flatfield.

The rather simple idea of illuminating the instrument with a homogeneous light source is limited in practice by the fact that it is almost impossible to find a truly-homogeneous light source (or, equivalently, a source with an accurately known spatial variation). For imaging solar instruments, the time-averaged quiet Sun qualifies as a light source with a fairly well-known spatial variation of the intensity (*i.e.*, the limb darkening function), but in the presence of active regions flatfields cannot be derived by simply adding up frames. One approach to obtain flatfields directly from solar images is to mask out active regions. Potts and Diver

R. Wachter (✉) · J. Schou
Hansen Experimental Physics Laboratory, 452 Lomita Mall, Stanford, CA 94305-4085, USA
e-mail: richard@sun.stanford.edu

(2008) produced MDI high-resolution flatfields by using simultaneous magnetograms to cut out active regions before averaging the frames.

In this paper, we present a method that uses regular-observation data to obtain the flatfield. Although the method of rotational flatfields is more general, we present an algorithm that is customized to monitor the small-scale flatfield of the upcoming *Helioseismic and Magnetic Imager* (HMI). Its performance is demonstrated using similar data sets from the *Michelson Doppler Imager* (MDI) (Scherrer *et al.*, 1995).

Space instruments suffer from cosmic-ray hits that can lead to permanent radiation damage of single pixels or neighboring pixels. The damage leads to pixels with permanently low gain. Schou (2004) investigated the radiation damage suffered by MDI from 1996 through 2003 and found pixels with a drop in gain of more than 20%. The damage accumulates over the lifetime of the mission. The flatfield can also change from outgassing and condensation at the CCD, in particular at the beginning of the mission. "Monitoring" the flatfield using ordinary observation data can provide a periodic update to the small-scale flatfield. HMI requires a high precision in the small-scale flatfield, as filtergrams have to be interpolated spatially to make observables. Our goal is to determine the small-scale flatfield to an accuracy of 0.1%, in line with the specifications for the HMI instrument.

The method developed by Kuhn, Lin, and Loranz (1991) does not rely on a homogeneous light source, but instead offsets the field of view in different directions and magnitudes to separate the spatial variation of the light source from the spatial variation of the instrumental response: relatively few frames are sufficient to obtain a reliable flatfield on small and large scales. The underlying assumption that the Sun does not change while the sequence of images is recorded is easily violated and represents a major source of noise in the offset flatfields. For MDI and HMI, the field of view can be offset either by moving the spacecraft, or by using the piezo-electric transductors (PZT). Moving the spacecraft can be rather slow on the time-scale of solar granulation, while the PZT can only provide small offsets, leaving the large-scale flatfield poorly constrained.

The rotational flatfielding presented in this paper does not require offpointing, but instead relies on the rotating Sun providing a natural offset of the solar pattern.

In order to make rotational flatfields, the data sets used for flatfielding need to meet the following requirements:

i) The data set must be a set of identical intensity images, preferably recorded at regular cadence, as an irregular cadence increases the computational burden substantially. Data gaps are acceptable as long as there are enough pairs of images with a constant time difference. The cadence must be substantially shorter than the lifetime of the imaged solar structure.

ii) The field of view must be the same for each pair of valid frames. Jumps in the field of view are acceptable as long as there are enough pairs of images with the same field of view.

iii) The Nyquist criterion must be fulfilled, *i.e.*, the sampling must comply with the spatial cutoff frequency set by the Modulation Transfer Function.

2. Solar Rotation

The rotational flatfields require *a-priori* knowledge of the rotational shifts in the image plane. The projection of the rotational shift onto the image plane depends on the location of the observing instrument with respect to the solar rotation axis, and it is therefore a function of the B angle and the P angle. We will consider both the B angle and the P angle to be

constant during the time the data set under consideration is obtained. This will put certain constraints on the maximum length of the data sets used.

Solar rotation in the image plane is a two-dimensional vector field which will be calculated using ephemeris data and information about the roll angle, the image scale, and the pointing of the instrument. Also, a model for the differential rotation needs to be applied.

It is important to note that the rotational shift becomes small towards the limb of the disk. For zero B angle, it vanishes altogether. The constraint on the rotational flatfield is therefore expected to become poor towards the limb.

The rotational shift over the regular 60-second cadence of MDI high-resolution data at disk center is roughly one-fourth of a pixel. The small shift is the reason that the large scales of the rotational flatfield are basically unconstrained. For HMI, we get a similar shift at disk center.

3. Equations

We follow Kuhn, Lin, and Loranz (1991) in considering the logarithm of the signal instead of the signal itself. As will become evident below, linearly interpolating in the logarithm instead of the quantity itself simplifies the calculations considerably, while the systematic error introduced is much lower than 0.1% for flatfield values within 40% of unity.

We consider two neighboring frames, k and $k+1$, and match them by shifting one of the frames spatially to compensate for solar rotation in the time between the two exposures. The limb-darkening corrected[1] signal at pixel $\{i, j\}$ in a given frame k can be expressed in terms of the following frame $k+1$:

$$S^k_{i,j} = \gamma_{00} S^{k+1}_{i,j} + \gamma_{10} S^{k+1}_{i+d_x,j} + \gamma_{01} S^{k+1}_{i,j+d_y} + \gamma_{11} S^{k+1}_{i+d_x,j+d_y}. \tag{1}$$

Conversely, shifting the earlier frame to the position of the later, we obtain

$$S^{k+1}_{i,j} = \gamma_{00} S^{k}_{i,j} + \gamma_{10} S^{k}_{i-d_x,j} + \gamma_{01} S^{k}_{i,j-d_y} + \gamma_{11} S^{k}_{i-d_x,j-d_y}. \tag{2}$$

Here, d_x and d_y are $+1$ and -1 depending on the direction of rotation in the horizontal and vertical direction, and the linear interpolation coefficients are given by

$$\begin{aligned} \gamma_{00} &= (1-r_x)(1-r_y), \\ \gamma_{01} &= (1-r_x) r_y, \\ \gamma_{10} &= r_x (1-r_y), \\ \gamma_{11} &= r_x r_y, \end{aligned} \tag{3}$$

where r_x and r_y are the absolute value of the horizontal and vertical rotational shift in pixels. We note that d_x and d_y generally depend on location for non-zero B-angle. All equations in this paper assume a sub-pixel rotational shift, as is the case for HMI and MDI. A generalization to shifts with more than one pixel is possible, although it alters the structure of the equations as well as the constraints on the flatfield. Equations (1) and (2) basically contain

[1] Note that the limb darkening correction is only important where the limb darkening function is sufficiently steep. For disk – center data such as MDI high resolution data, it can be neglected.

the same information, but using both equations makes the system symmetric in the direction of rotation. The logarithm of the solar signal is given by

$$S^k_{i,j} = D^k_{i,j} - G_{i,j}, \tag{4}$$

where $D^k_{i,j}$ is the logarithm of the dark-subtracted and limb-darkening corrected raw signal, and $G_{i,j}$ is the logarithm of the gain.

Combining Equation (4) with Equations (1) and (2) leads to

$$\begin{aligned}&(\gamma_{00}-1)G_{i,j} + \gamma_{10}G_{i+d_x,j} + \gamma_{01}G_{i,j+d_y} + \gamma_{11}G_{i+d_x,j+d_y}\\ &\quad= \gamma_{00}D^{k+1}_{i,j} + \gamma_{10}D^{k+1}_{i+d_x,j} + \gamma_{01}D^{k+1}_{i,j+d_y} + \gamma_{11}D^{k+1}_{i+d_x,j+d_y} - D^k_{i,j},\end{aligned} \tag{5}$$

and

$$\begin{aligned}&(\gamma_{00}-1)G_{i,j} + \gamma_{10}G_{i-d_x,j} + \gamma_{01}G_{i,j-d_y} + \gamma_{11}G_{i-d_x,j-d_y}\\ &\quad= \gamma_{00}D^{k}_{i,j} + \gamma_{10}D^{k}_{i-d_x,j} + \gamma_{01}D^{k}_{i,j-d_y} + \gamma_{11}D^{k}_{i-d_x,j-d_y} - D^{k+1}_{i,j}.\end{aligned} \tag{6}$$

Note, that the left-hand side of both equations is independent of the data. This is the benefit of using the logarithmic quantities.

The linear Equations (5) and (6) can also be written in matrix form:

$$A_1\mathbf{g} = \mathbf{b}^k_1, \tag{7}$$

$$A_2\mathbf{g} = \mathbf{b}^k_2, \tag{8}$$

where A_1 and A_2 are block – bidiagonal matrices of size $n_\mathrm{p} \times n_\mathrm{p}$ (with n_p being the number of pixels in the array), $\mathbf{g}$ is the vector containing all components $G_{i,j}$, and $\mathbf{b}^k_1$ and $\mathbf{b}^k_2$ are the vectors representing the corresponding right-hand side of Equations (5) and (6).

The flatfield is obtained from the vector $\mathbf{g}$ that minimizes the expression:

$$\left\{\sum_k \left\|A_1\mathbf{g} - \mathbf{b}^k_1\right\|^2 + \left\|A_2\mathbf{g} - \mathbf{b}^k_2\right\|^2 + \lambda||\mathbf{g}||^2\right\}. \tag{9}$$

We added a L^2 norm regularization controlled by the parameter λ. The regularization forces the unconstrained additive constant in G to zero (thereby ensuring a mean flatfield of one) and acts as a high-pass filter to the flatfield. The regularization needs to be carefully adjusted to the data and the flatfield, as a higher regularization parameter both decreases the variance and increases the bias of the estimated flatfield.

The solution to the least-square problem satisfies the equation:

$$n\left(A_1^\mathrm{T}A_1 + A_2^\mathrm{T}A_2 + \lambda' I\right)\mathbf{g} = A_1^\mathrm{T}\sum_k \mathbf{b}^k_1 + A_2^\mathrm{T}\sum_k \mathbf{b}^k_2, \tag{10}$$

where k runs over all frames for which both frames k and $k+1$ are valid, n is the number of all valid pairs of frames in the data set, I is the identity matrix, and $\lambda' = \lambda/n$. The suppression of low frequencies is controlled by the parameter λ'.

4. Numerical Solution

For HMI, Equation (10) is a system of about 11.7 million linear equations[2] and as many unknowns. In order to solve it efficiently, we need to take advantage of the particular structure of the matrix of coefficients.

It has a block – tridiagonal structure, with each block representing a row (or a column) of pixels, and is solved using a block relaxation method, which works analogously to the Gauss – Seidel relaxation method, but instead of one pixel it solves for one row (or one column) at a time, and iteratively propagates the solution in the perpendicular direction. For each row, the problem reduces to solving a tridiagonal linear system, for which effective standard solutions exist ("Thomas Algorithm").

As HMI might operate at different P angles at times, we need to make sure that the code runs for all P angles. As the solar rotation introduces a preferred direction, an alignment of the rows (or columns) of the CCD with the direction of rotation leads to the best convergence. This can be achieved for P angles of 0° and 90°. For P angles above 45°, we exchange the indices for rows and columns. For P angles far from the horizontal and vertical, the convergence can be slower by orders of magnitude. Using a Simultaneous Overrelaxation Method (Hageman and Young, 1981, see also Toussaint, Harvey, and Toussaint, 2003) for application to a flatfielding algorithm) helps to speed up the convergence. We found that the optimal overrelaxation parameter is a strong function of the P angle, with higher values working better for P angles far from the horizontal or vertical.

5. Tests with MDI Data

5.1. MDI Continuum Intensity

We tested the algorithm with MDI high-resolution intensity data. The level-zero continuum intensity ("I0") data represent one of the five MDI filtergrams. For HMI, all filtergrams will be available all of the time. Continuum intensity data are abundant and resemble the HMI filtergrams both in spatial resolution and cadence. However, they are restricted to the center of the disk. We note that MDI full-disk data are severely undersampled, so they cannot be used to produce rotational flatfields. As an unfortunate consequence, we cannot test the performance of the rotational-flatfield algorithm near the limb, which will be important for HMI.

We calculated the flatfield of two temporally-adjacent data sets, each containing about 450 frames, and a data set of the same length ten month later. The difference of the flatfields from the adjacent data sets serves as an estimate for the noise. The difference of the time-separated flatfields gives information about the change in the flatfield in the meantime.

Figure 1 shows the histogram of the difference of the flatfields. The tail of the Gaussian distribution represents the pixels with a substantial loss in gain. For the difference of the near-contemporal flatfields which provides an estimate of the solar noise, we see a Gaussian distribution with a width of roughly 0.16%. The widening of the Gaussian part of the distribution with time points towards small scale, but large-area flatfield changes also.

Assuming that just a few pixels change gain between two flatfields, we can derive a detection limit for a pixel changing its gain. Assuming the noise to be spatially homogeneous,

[2]There is no rotational flatfield for pixels beyond the limb. A certain number of pixels inside the limb also have to be cropped, because the rotational shift is too low there.

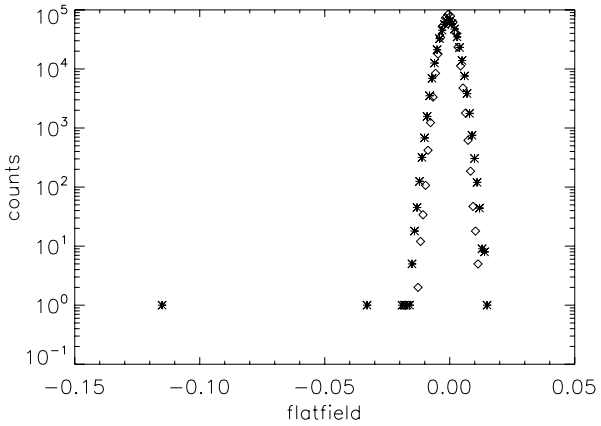

Figure 1 Histogram of the difference of the two flatfields from data sets ten months apart (stars), and the difference from two flatfields from the same day in June 1999 (diamonds). The Gaussian distribution of the diamonds reflects the solar noise in the flatfields, because the flatfield can be assumed to be unchanged within such a short time. The stars show the flatfield change after ten months. There are at least two pixels with a substantial loss in gain, and a slight increase in the width of the Gaussian, indicating a minor small scale flatfield change on a large area.

we can derive a probability density function for a given flatfield value occurring at a single pixel as part of the normal noise distribution. Doing so, we obtain an implicit expression for the detection limit (l), above which a pixel can be considered having undergone a substantial change in gain:

$$\left(\mathrm{erf}\left(\frac{l}{\sqrt{2}\sigma}\right)\right)^{n_\mathrm{p}} = 1 - p, \tag{11}$$

where erf is the error function, σ is the standard deviation of the noise, and p is the residual probability of a spurious detection.

If we set p to 1%, we obtain a detection limit of 5.6 σ or 0.90% for the given array of half a million pixels.

We note that σ decreases with a higher regularization parameter. However, the regularization parameter needs to be small enough to not introduce any substantial bias above the required limit of accuracy.

In order to determine the scale beyond which the flatfields are noise dominated, we compare the power spectrum of the flatfields which are derived from time-adjacent data sets. In Figure 2 we show the power spectrum in the horizontal direction (*i.e.*, the direction of rotation), the vertical direction for the flatfield, and the power of the ratio of the two flatfields. As the two flatfields are supposed to be identical, their ratio should show little power compared to the flatfield itself. The signal-to-noise ratio is only high for the very small scales. Details depend on the length of the data set and the tuning of the regularization parameter. A good signal-to-noise ratio is important to obtain a reliable "secondary flatfield". A "secondary flatfield" is derived from data already flatfielded with an existing flatfield. With MDI, we have observed not only isolated pixels going bad, but also small-scale flatfield changes on larger areas, possibly a result of condensation on the CCD. Should anything similar be observed during the HMI mission, we plan to apply a high-pass-filtered rotational flatfield as a secondary flatfield.

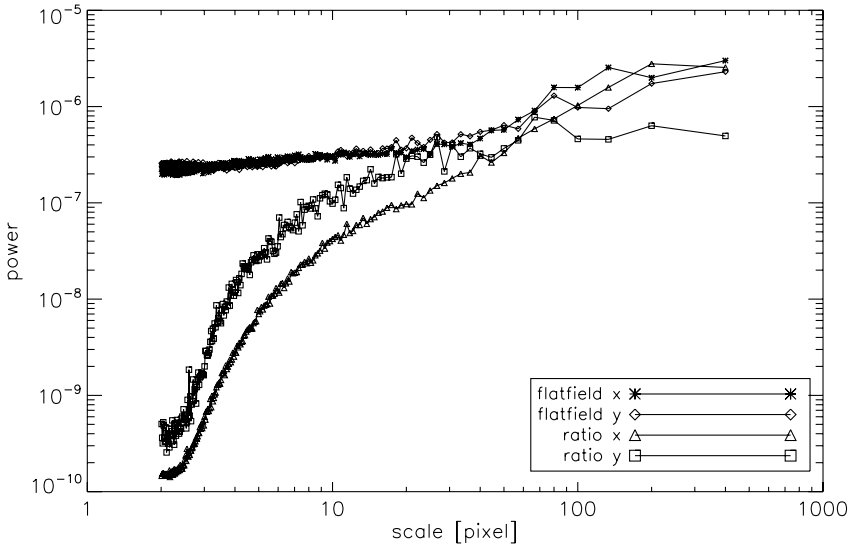

Figure 2 Power spectrum of the flat field in the horizontal and vertical directions (where the horizontal axis is the fast scan axis and the vertical axis is the slow scan axis) and the power of the solar noise in the flatfield obtained from two data sets close in time. The signal-to-noise ratio is high only on the very short scales of a few pixels. The spatial scale is defined as $2\pi/k$, where k is the magnitude of the wave number in the 2D Fourier transform.

5.2. MDI Line-Profile Campaigns

So called "line profile campaigns" downlink all of the filtergrams for a limited area of the MDI CCD. In the unbinned version, we have a 256×256 field for a chosen section within the high-resolution field of view. These campaigns are of interest, because they closely resemble the HMI data with all filtergrams available, although on a much smaller field of view.

The noise in the flatfields is largely of solar origin. Therefore, if we derive a flatfield for each filtergram separately, the noise in each of them is highly correlated. The noise level turns out to be higher for the filtergrams near the line center, which show a more rapid variation in time. The flatfield on small scales is dominated by the CCD, and it should therefore be the same for all filtergrams. First, we estimate the noise in each filtergram from a 14-hour-long data set from April 2005. The data are divided in two chunks of equal length, and the root-mean-square of the difference of the flatfields is a measure of the noise level. The right panel of Figure 3 shows the covariance matrix of the noise. Given the covariance matrix and the flatfields for the individual filtergrams, the optimally weighted average is given by

$$\bar{\mathbf{g}} = \frac{\sum_{f,f'} \Gamma_{f,f'} \mathbf{g}_{f'}}{\sum_{f\,f'} \Gamma_{f,f'}}, \tag{12}$$

where the $\mathbf{g_f}$ are the flatfields derived from the different filtergrams, Γ is the inverse of the covariance matrix, and $\bar{\mathbf{g}}$ is the optimally averaged flatfield.

The left panel of Figure 3 shows how the noise level in the different filtergrams varies. Near line center, the signal samples a higher level in the atmosphere, and the filtergrams are strongly affected by the Doppler shift of the line.

The optimally weighted average shows only a marginal improvement of a few percent compared to the single filtergram flatfield which has the lowest noise level (*i.e.*, the con-

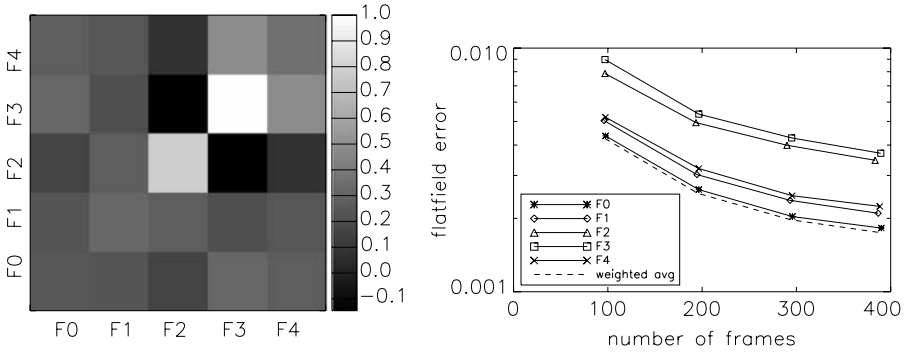

Figure 3 Left panel: Covariance matrix of the noise in the flatfields obtained from different filtergrams. The noise is estimated from the difference of two flatfields derived from temporally adjacent data series. The values of the covariance matrix have been normalized to the maximum value. Right panel: Noise level in the flat field as a function of the number of frames. The noise falls off with the square root of the number of frames. The filtergrams show a very different noise level. As the noise is highly correlated, the improvements from an optimally weighted average (lowest graph) are minor.

tinuum filtergram). This is because the errors in the near continuum filtergrams, where the noise level is low, are highly correlated and do not provide independent information, whereas the filtergrams near line center, where the noise is largely independent have a substantially higher noise and consequentially get a lower weight in the average. Figure 3 also demonstrates that the noise is dominated by the varying solar structure, not by the photon noise, which is about one magnitude smaller.

6. HMI Flatfield Monitoring

HMI will record Dopplergrams, line-of-sight magnetograms, and continuum intensity at a cadence of 45 – 50 seconds, while the vector magnetic field is recorded at a lower cadence. This implies that one of the two HMI cameras will record identical filtergrams every 45 – 50 seconds, while the other camera may repeat identical filtergrams on a lower cadence.

As the small scales are dominated by the CCD flatfield features, we assume all filtergrams to have the same small scale flatfield. After the flatfield has been retrieved from the filtergram, we look at the difference of the rotational flatfield and a reference flatfield, which can be either an offset flatfield or the previous rotational flatfield. The histogram of the difference will be Gaussian reflecting the noise that can be attributed to the time-varying solar structure. Applying expression (11) to the number of illuminated pixels on HMI, we obtain a detection limit of 6.1σ. Extrapolating the results we obtained from MDI, one day of data results in a detection limit for bad pixels of 0.5%. Therefore, we expect to meet the nominal requirement for HMI, *i.e.*, a root-mean-square accuracy of the flatfield of 0.1%, using one day of data. One month of data will bring us below a single-pixel accuracy of 0.1%, but changes in the roll angle might prevent us from using very long data series. Also, the pace and extent of the flatfield change will determine the length of the data series used for the flatfield correction. Once a pixel has been identified as loosing gain within a given period of time, it is straightforward to pin down the very moment of the pixel going bad, at least if the drop exceeds the variation of the solar signal of $\approx$2% (see Schou, 2004).

If a more steady change of the small scale flatfield over large areas is observed, we intend to apply a "secondary flatfield". Undoubtedly, it will be a source of noise, but it will improve

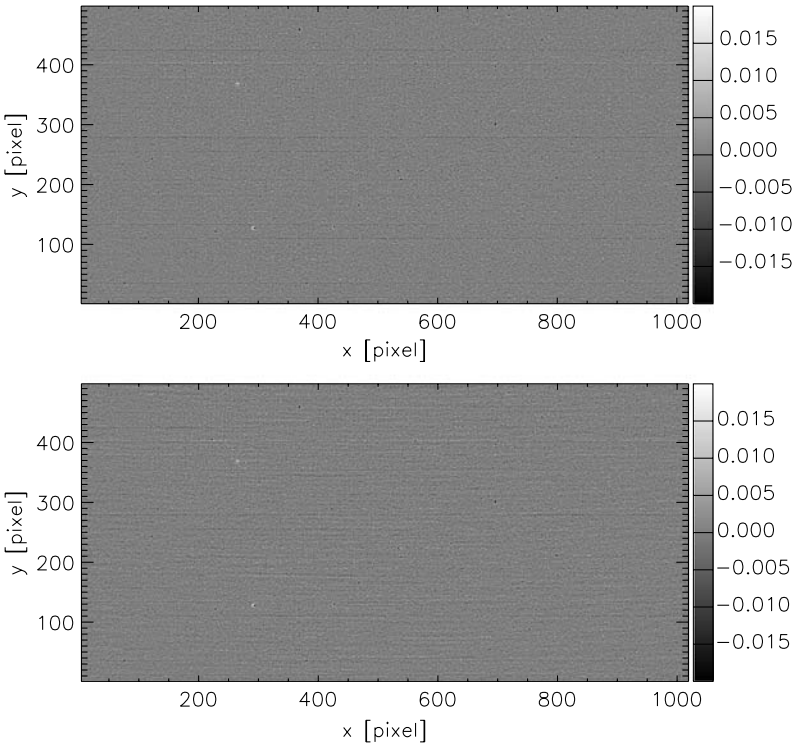

Figure 4 Average flatfield (upper panel), and the rotational flatfield (lower panel). The color scale has been saturated to better show the spatial structure. The data set used for this plot contained close to 2000 frames, comparable to a day of HMI data. Both flatfields have been filtered with a FWHM of three pixels high-pass filter. The flatfields show the horizontal structure of the CCD and isolated low-gain pixels, which produce a small ringing-pattern when the high-pass filter is applied.

the flatfield if the amplitude of the secondary flatfield is significantly above the noise level. Pixels gone bad will be large spikes in the secondary flatfield, so in order to avoid any ringing effects in the neighborhood of the spikes, we need to isolate them first before the high-pass filter is applied.

We note that the performance of the algorithm on HMI data cannot be fully inferred from MDI data. The data will be taken in a different absorption line (which will affect the noise level of the flatfields from the different filtergrams), and the cadence will be higher or lower, depending on the frame list that will be used. HMI data from the ground are not suitable because of strong atmospheric disturbances.

7. Average Flatfield versus Rotational Flatfield

We compare the rotational flatfield with a flatfield derived from frame-averaging. We applied the rotational flatfield method to a data set that has been used by Potts and Diver (2008) to obtain average flat fields.

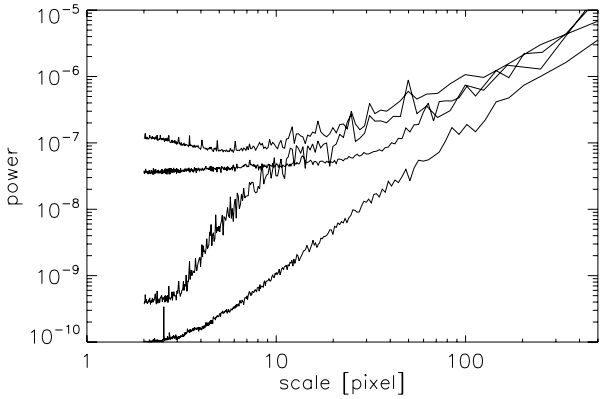

Figure 5 The horizontal and vertical power spectra of the rotational flatfield, and the power of the ratio of the rotational and the average flatfield. From top to bottom at the left-hand side of the graph, the lines represent the power in the vertical direction, the power in the horizontal direction, the power of the ratio in vertical direction, and the power of the ratio in horizontal direction. The peaks in the power of the vertical direction are a consequence of the structure of the CCD. Note that the rotational flatfield is better constrained in the horizontal direction, which is the main direction of rotation.

Figure 4 shows the two flatfields on small scales.[3] The horizontal lines reflect the structure on the CCD, which is also visible in the (nominal) offset flatfields. Figure 5 shows the power spectrum of the rotational flatfield and the power spectrum of the ratio of a rotational flatfield and an average flatfield.

A (limb-darkening corrected) average flatfield has the clear advantage of giving a reliable flat field on all scales. When the Sun is free of activity, it can be used as a calibration standard for the rotational flatfield to tune the regularization parameter and perform an adequate frequency filtering. Figure 5 shows that the rotational flatfield and the average flatfield agree very well on scales below three pixels (where the spatial scale is defined as the inverse wavelength). The disadvantage of the average flatfield is that the active regions have to be removed in a sometimes tedious way, and the noise level in the flatfield is spatially very inhomogeneous as the number of averaged frames depends on the location on the CCD. Rotational flatfields sometimes show traces of activity, but these traces are generally small enough to not interfere with the detection of pixels that lost gain. Although the formalism of the rotational flatfields involves the solution of a linear system after adding up frames, the additional computational burden is low as solving the linear equations is efficient and independent of the length of the data set. Unlike frame-averaging flatfields, no pixel selection is required. Rotational flatfields are therefore a good choice to regularly monitor the flatfield for continuous solar observation like HMI, if only the short scale flatfield is of interest.

8. Conclusion

We developed a method to obtain small-scale flatfields from raw solar intensity images using solar rotation. The method has been developed for the upcoming *Helioseismic and Magnetic Imager*, and has been demonstrated using MDI High Resolution data.

[3]The flatfields published in Potts and Diver (2008) are secondary flatfields produced from level 1.5 data. In order to make them comparable to the rotational flatfields of this paper, they have to be multiplied by the primary flatfield which is applied to calibrated MDI data.

The method is suitable for detecting and correcting gain reductions which occur randomly due to the radiative environment in space. It can also be used to obtain secondary flatfields in between the spacecraft offset flatfield and the PZT flatfields. The required accuracy of 0.1% can most likely be reached for the root-mean-square of the flatfield, but not for single pixels. The method can be used for other imaging solar instruments with a fixed field of view and regular cadence.

The method can be applied to other imaging solar space instruments, in particular photospheric imagers (*e.g.*, the *Hinode*/NFI and BFI images). The method could also be applied to ground-based instruments, but the atmospheric perturbations will probably drive up the noise level substantially.

Acknowledgements This research is supported by NASA contracts NNX07AK36G and NAS5-02139. SOHO is a mission of international collaboration between ESA and NASA. The authors thank Rasmus Munk Larsen for his valuable comments and support.

References

Hageman, L.A., Young, D.M.: 1981, *Applied Iterative Methods*, Academic Press, New York.

Kuhn, J.R., Lin, H., Loranz, D.: 1991, Gain calibrating nonuniform image-array data using only the image data. *Publ. Astron. Soc. Pac.* **103**, 1097 – 1108. doi:10.1086/132932.

Potts, H.E., Diver, D.A.: 2008, Post-hoc derivation of SOHO Michelson Doppler imager flat fields. *Astron. Astrophys.* **492**, 863 – 871. doi:10.1051/0004-6361:200810606.

Scherrer, P.H., Bogart, R.S., Bush, R.I., Hoeksema, J.T., Kosovichev, A.G., Schou, J., Rosenberg, W., Springer, L., Tarbell, T.D., Title, A., Wolfson, C.J., Zayer, I., MDI Engineering Team: 1995, The solar oscillations investigation – Michelson Doppler Imager. *Solar Phys.* **162**, 129 – 188.

Schou, J.: 2004, SOHO MDI CCD performance. In: Favata, F., Aigrain, S., Wilson, A. (eds.) *Stellar Structure and Habitable Planet Finding* **SP-538**, ESA, Noordwijk, 411 – 415.

Toussaint, R.M., Harvey, J.W., Toussaint, D.: 2003, Improved convergence for CCD gain calibration using simultaneous-overrelaxation techniques. *Astron. J.* **126**, 1112 – 1118. doi:10.1086/376846.